





# DC Current Suppression in CHB-STATCOM With Model Predictive Control Employing Current Transformers

Francesco Simonetti , *Student Member, IEEE*, Sobhan Mohamadian , *Member, IEEE*, Concettina Buccella , *Fellow, IEEE*, and Carlo Cecati , *Life Fellow, IEEE*

**Abstract**—DC current injection is a common problem in grid-tied inverters and it is especially emphasized when current transformers are employed to sense the current. Although the dc current elimination is already addressed for linear controllers, it is not faced for model predictive control. This manuscript proposes a dc current elimination strategy for cascaded H-bridge (CHB) static synchronous compensators controlled by finite control set model predictive control (FCS-MPC). In addition to the two optimization layers of typical FCS-MPC, this article proposes using a third optimization layer to balance the voltages of the clusters. This article demonstrates that the dc current is suppressed by minimizing the imbalance among the clusters through the common-mode voltage. The algorithm is simple to implement and the ac output current is not affected. Validation is carried out with a five-level CHB-STATCOM, and a classical approach is compared.

**Index Terms**—Cluster balancing, current transformer, dc current elimination, model predictive control (MPC), multilevel inverters, static synchronous compensator (STATCOM).

## NOMENCLATURE

$\mathbf{i}_{\alpha,\beta}^{\text{ref}}$	Output current reference vector in $\alpha, \beta$ frame.
$\mathbf{i}_{\alpha,\beta}$	Output current vector in $\alpha, \beta$ frame.
$\mathbf{Q}_{cb}$	Weight matrix for voltages in clusters voltages control.
$\mathbf{Q}_{ib}$	Weight matrix for voltages in individual voltages control.
$\mathbf{Q}_i$	Weight matrix for current in current control.

$\mathbf{R}_{cb}$	Weight matrix for switching frequency in clusters control.
$\mathbf{R}_{ib}$	Weight matrix for switching frequency in voltages control.
$\mathbf{R}_i$	Weight matrix for switching frequency in current control.
$\mathbf{S}_{\alpha,\beta}^*$	Optimal switching vector in $\alpha, \beta$ frame.
$\mathbf{S}_{a,b,c}^*$	Optimal switching vector in $a, b, c$ frame.
$\mathbf{S}_{\alpha,\beta}$	Switching vector in $\alpha, \beta$ frame.
$\mathbf{S}_{a,b,c}$	Switching vector in $a, b, c$ frame.
$\mathbf{s}_p$	Individual switching signals vector of phase $p$ .
$\mathbf{T}$	Clarke transform matrix.
$\mathbf{V}^{\text{DC}}$	Reference voltages vector for individual voltages control.
$\mathbf{V}_{a,b,c}^{\text{DC}}$	Reference voltages vector for clusters voltages control.
$\mathbf{V}_{\alpha,\beta}$	Set of feasible switching vectors in $\alpha, \beta$ frame.
$\mathbf{V}_{a,b,c}$	Set of feasible switching vectors in $a, b, c$ frame.
$\mathbf{v}_{C(a,b,c)}$	Clusters voltages vector.
$\mathbf{v}_{Cp}$	Capacitors individual voltages vector of phase $p$ .
$\mathbf{v}_{s(\alpha,\beta)}$	Grid voltage vector in $\alpha, \beta$ frame.
$\omega$	Grid angular speed.
$\phi_{Ic}$	Phase of the line-frequency component of $i_{Cp}$ .
$\phi_I$	Phase of the line-frequency component of $i_p$ .
$\phi_S$	Phase of the line-frequency component of $S_p$ .
$\tilde{S}$	Amplitude of the constant component of $S_p$ .
$\tilde{I}_S$	Amplitude of the constant component of $i_p$ .
$\bar{v}_C$	Average capacitors voltage.
$\tilde{I}_C$	Amplitude of the line-frequency component of $i_{Cp}$ .
$\tilde{I}_S$	Amplitude of the line-frequency component of $i_p$ .
$\tilde{S}$	Amplitude of the line-frequency component of $S_p$ .
$C$	DC-link capacitance.
$C_{eq}$	Cluster capacitance.
$i_p$	Output current of phase $p$ .
$i_{Cp}$	Cluster current in the dc side of phase $p$ .
$i_{lp}$	Cluster loss current in the dc side of phase $p$ .
$k$	Sampling instant.
$L$	Inductance of the filter inductance.
$n$	Number of H-bridges per phase.
$R$	Resistance of the filter inductance.
$s_{pi}$	Individual switching signal of $i$ th H-bridge of phase $p$ .

Manuscript received 4 June 2023; revised 16 October 2023; accepted 5 December 2023. Date of publication 17 January 2024; date of current version 19 June 2024. This work was supported in part by NEST-PNRR MUR – M4C2 - I 1.3 under Grant D93C22000900001. The converter was developed by DigiPower Ltd., L'Aquila, Italy, in part under Grant "HORIZON 2020" PON I&C2014-2020, No. F/050220/X32 CUP B18115000100008. (Corresponding author: Francesco Simonetti.)

Francesco Simonetti, Sobhan Mohamadian, and Concettina Buccella are with the Department of Information Engineering, Computer Science and Mathematics, University of L'Aquila, 67100 L'Aquila, Italy (e-mail: francesco.simonetti1@graduate.univaq.it; sobhan.mohamadian@univaq.it; concettina.buccella@univaq.it).

Carlo Cecati is with the Politecnico di Bari, 70126 Bari, Italy (e-mail: c.cecatti@iee.org).

Color versions of one or more figures in this article are available at <https://doi.org/10.1109/TIE.2023.3342302>.

Digital Object Identifier 10.1109/TIE.2023.3342302

$s_{pi}^*$	Optimal switching signal of $i$ th H-bridge of phase $p$ .
$S_p$	Switching vector of phase $p$ .
$S_p^*$	Optimal switching vector of phase $p$ .
$T_s$	Sampling interval length.
$v_{Cpi}$	Individual dc-link voltage of $i$ th capacitor of phase $p$ .
$v_{Cp}$	Cluster voltage of phase $p$ .
$v_{sp}$	Output voltage of STATCOM of phase $p$ .
$V_{DC}$	DC-link rated voltage.

## I. INTRODUCTION

**G**RID-TIED converters, such as flexible ac transmission systems (FACTSs) or photovoltaic inverters, inject/absorb ac power to/from the grid [1]. Power quality standards fix strict limits to the injected dc current because they increase the losses in distribution transformers, corrode network cabling, and lead to safety issues and saturation of magnetic cores. The imposed limit varies depending on the country. USA and China tolerate 0.5% of the rated output current, U.K. and Australia allow 5 mA, while Germany accepts 1-A dc current [2]. DC current injection is caused by asymmetry in gate signals or power transistors outputs, errors in the analog-to-digital converters (A/D), zero-drifting in sensors and signal conditioning circuits [2]. These shortcomings can be attenuated by improving the measuring circuit or adding a line-frequency transformer between the converter and the grid, increasing the overall losses of the structure, size, and cost. The worst situation arises when using current transformers (CTs), popular sensors due to their galvanic insulation and electromagnetic capability, ability to deal with large inrush currents and low cost. However, since they are based on the electromagnetic coupling principle, they cannot measure the dc component of the circulating current [3]. As a result, a closed-loop control can only stabilize the ac current, ignoring the dc component.

Adopted solutions for detecting and suppressing the dc current usually require the use of extra hardware [4], [5], [6], [7]. For instance, in [5], an additional current sensor is added to the dc-link of a transformer-less H-Bridge to detect the dc offset in the output phase currents by measuring the dc-link current during the freewheeling intervals of the unipolar pulse width modulation (PWM) scheme. In [6], the authors proposed a combination of hardware, including an isolated  $RC$  attenuation circuit, and software, an estimation scheme through a dc component filtering algorithm, for a single-phase PV inverter. In [7], the CT is equipped with a power amplifier, an additional winding, and a commercial current sensor. The output of the extra sensor is filtered to obtain the dc component used in the closed-loop control. In order to reduce the costs of additional hardware, software-based solutions have been presented in literature [8], [9], [10], [11], [12]. In [9], the dc current injected by a static synchronous compensator (STATCOM) [13] employing CTs is estimated by filtering the line-frequency ripple on the capacitors with a moving average filter (MAF). A proportional–integral (PI) regulator was added to the standard control scheme [14], [15] to compensate for the detected dc current. In [10], the dc current injected by a grid-tied inverter is attenuated by controlling the

dc component of the output voltage. A PI-based control scheme is employed to compute  $d, q$  currents to compensate for this dc voltage. In [11], a proportional–integral–resonant (PIR) controller is proposed to eliminate the dc current of a single-phase PV inverter, which is estimated from the line-frequency ripple of the dc-link voltage. There is a correlation between the dc current injected by the inverter in the grid and the line-frequency ripple on the dc-link voltage [12].

In the control of cascaded H-bridge STATCOMs (CHB-STATCOM), which this work is referred to, the use of a control scheme for balancing the dc-link voltage of the three phases is commonly employed [16], [17], [18]. The same approach is also used in finite control set model predictive control (FCS-MPC or direct MPC), which became a popular control technique for power converters during the last decades [19], [20], [21], [22], [23].

In CHB-STATCOM, the control problem is typically divided into two subproblems, i.e., current control and voltages balancing problem [24], [25], [26], [27]. Moreover, a third optimization can be added to control the voltages of the clusters [21], [22]. In [26], the voltage vector in the  $a, b, c$  domain is selected by searching among the redundant vectors to balance the voltages of the clusters. In [21], the voltages of the clusters are predicted to compute the zero-sequence voltage to inject for balancing them.

This article proposes using a cluster balancing strategy for the FCS-MPC of CHB-STATCOM to suppress the dc current injected into the grid. Despite the topic was already addressed for liner controllers, to the best of the authors' knowledge, it was never faced for the MPC strategy. Through extensive theoretical and experimental analyses, this article demonstrates that the dc output current is suppressed by controlling the dc-link voltage of the clusters accomplished by injecting a common-mode voltage. The proposed approach does not require extra sensors and complex filtering procedures, it is simple to implement and computationally efficient. A five-level CHB-STATCOM employing CTs is used as a demonstrator for the proposed algorithm, validating its effectiveness [28]. A comparison with a standard PI approach is provided, underlying the differences and stating the advantages of the proposed technique.

## II. CASCADED H-BRIDGE STATCOM MODEL

A three-phase, CHB-STATCOM consists of  $n$  cascaded H-bridges per phase, each one with a dc-link capacitor  $C$ , and connected to the grid through a filter inductor  $L$  with internal resistance  $R$ , as shown in Fig. 1. The output voltage  $v_p$  of the phase  $p$  is given by the sum of the output voltages of each cell

$$v_p = \sum_{i=1}^n s_{pi} \cdot v_{Cpi} \simeq \sum_{i=1}^n s_{pi} \cdot V_{DC},$$

$$i = 1, \dots, n; p \in \{a, b, c\} \quad (1)$$

where  $V_{DC}$  is the nominal dc-link voltage for each cell,  $v_{Cpi}$  is the actual voltage of each and  $s_{pi} \in \{-1, 0, 1\}$  is the discrete switching variable which indicates whether the H-bridge is outputting negative, zero, or positive voltage. The discretized

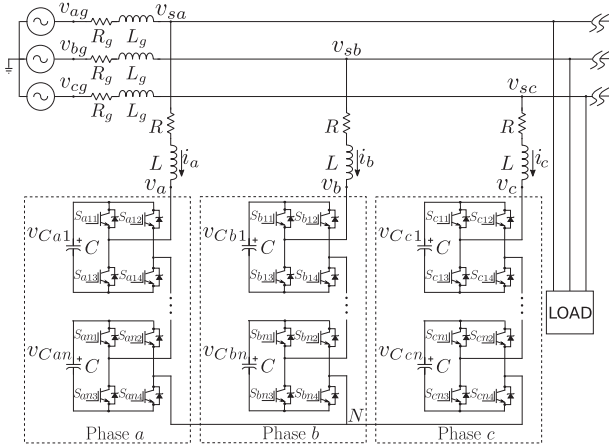


Fig. 1. Cascaded H-bridge STATCOM schematics.

equations of the currents and voltages in the stationary reference frame are

$$\mathbf{i}_{\alpha,\beta}(k+1) = \begin{bmatrix} 1 - \frac{T_s R}{L} & 0 \\ 0 & 1 - \frac{T_s R}{L} \end{bmatrix} \mathbf{i}_{\alpha,\beta}(k) + \begin{bmatrix} \frac{T_s}{L} & 0 \\ 0 & \frac{T_s}{L} \end{bmatrix} \mathbf{v}_{s(\alpha,\beta)}(k) - V_{DC} \begin{bmatrix} \frac{T_s}{L} & 0 \\ 0 & \frac{T_s}{L} \end{bmatrix} \mathbf{S}_{\alpha,\beta}(k) \quad (2)$$

$$v_{Cpi}(k+1) = v_{Cpi}(k) + \frac{T_s}{C} (s_{pi}(k) \cdot i_p(k))$$

$$p \in \{a, b, c\}, i = 1, \dots, n \quad (3)$$

where  $T_s$  is the sampling time,  $\mathbf{i}_{\alpha,\beta}$  is the  $\alpha, \beta$  current vector,  $\mathbf{v}_{s(\alpha,\beta)}$  the grid voltage vector, and  $\mathbf{S}_{\alpha,\beta}$  is the inverter switching vector in  $\alpha, \beta$  coordinates;  $i_p$  is the phase  $p$  current.

### III. MODEL PREDICTIVE CONTROL FOR CHB-STATCOM

The partially stratified approach is generally used to solve the FCS-MPC for CHB-STATCOM [24], [25], [26], [27], which divides the overall optimization problem into the current control and the individual voltage balancing problems. The first one aims to find the optimum switching vector  $\mathbf{S}_{\alpha,\beta}$  in  $\alpha, \beta$  frame by minimizing the tracking current error. The second one aims to find the switching variables  $s_{pi}$  that minimize the voltage imbalance among capacitors in the three phases. Generally, the  $a, b, c$  vector is computed by transforming  $\mathbf{S}_{\alpha,\beta}$ , setting the homopolar component equal to zero.

#### A. Current Control Problem

The dynamical model in (2) is employed in order to solve the following optimization problem:

$$\min_{\mathbf{S}_{\alpha,\beta}(k)} \left\| \mathbf{i}_{\alpha,\beta}^{\text{ref}}(k+1) - \mathbf{i}_{\alpha,\beta}(k+1) \right\|_{\mathbf{Q}_i} + \left\| \mathbf{S}_{\alpha,\beta}(k-1) - \mathbf{S}_{\alpha,\beta}(k) \right\|_{\mathbf{R}_i}$$

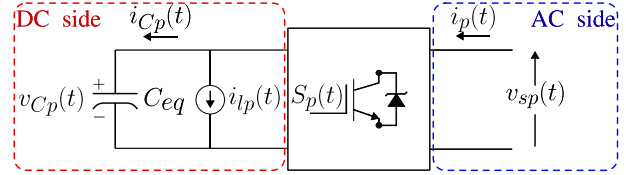


Fig. 2. Simplified individual cluster of the CHB-STATCOM.

s. t. (2),

$$\mathbf{S}_{\alpha,\beta}(k) \in \mathbf{V}_{\alpha,\beta} \quad (4)$$

where a tradeoff between the tracking accuracy of the reference current  $\mathbf{i}_{\alpha,\beta}^{\text{ref}}$  and the switching frequency is computed in every instant  $k$ . The  $2 \times 2$  weighting matrices  $\mathbf{Q}_i$  and  $\mathbf{R}_i$  are tuning parameters and the switching vector must belong to the set of feasible vectors  $\mathbf{V}_{\alpha,\beta}$ .

#### B. Individual Voltages Balancing Problem

The individual balancing control problem aims to select the individual H-bridges switching signals that realize the  $\mathbf{S}_{a,b,c}^*$ , while keeping the voltage balance among the dc-link capacitors. The optimization problem for the individual balancing of phase  $p \in \{a, b, c\}$  is the following:

$$\min_{\mathbf{s}_p(k)} \left\| \mathbf{V}^{\text{DC}} - \mathbf{v}_{Cp}(k+1) \right\|_{\mathbf{Q}_{ib}} + \left\| \mathbf{s}_p(k) - \mathbf{s}_p(k-1) \right\|_{\mathbf{R}_{ib}}$$

$$\text{s. t. } v_{Cpi}(k+1) = v_{Cpi}(k) + \frac{T_s}{C} (s_{pi}(k) \cdot i_p(k)),$$

$$i = 1, \dots, n$$

$$\sum_{i=1}^n s_{pi}(k) = S_p^*(k)$$

$$s_{pl} \cdot s_{pm} \geq 0 \quad \forall l, m = 1, \dots, n : l \neq m \quad (5)$$

where  $\mathbf{V}^{\text{DC}} = [V_{DC}, \dots, V_{DC}]^T$  and  $\mathbf{v}_{Cp} = [v_{Cp1}, \dots, v_{Cpn}]^T$  are the  $n \times 1$  vectors containing the reference voltages and individual voltages of phase  $p$ , respectively, while  $\mathbf{s}_p = [s_{p1}, \dots, s_{pn}]^T$  is the vector of individual switching signals. The matrices  $\mathbf{Q}_{ib}$  and  $\mathbf{R}_{ib}$  perform the tradeoff in the optimization; the constraints ensure that the overall switching vector is the one computed in the current control layer.

### IV. DC CURRENT INJECTION PROBLEM AND SOLUTION

This work proposes adding a third optimization layer between the first two, aiming to reduce the imbalance among the three clusters and to remove the injected dc current by controlling the output common-mode voltage of the STATCOM.

#### A. Link Between DC Current and Capacitor Voltage

It is well known in literature that, by using CT sensors, a dc current is generated at the output of the STATCOM [9]. Fig. 2 shows a simplified model of the individual cluster of the

STATCOM. The relationship between the current on the ac side  $i_p(t)$  and the dc-link voltage  $v_{Cp}(t)$  is

$$C_{eq} \frac{dv_{Cp}(t)}{dt} = i_{Cp}(t) = S_p(t) \cdot i_p(t) - i_{lp}(t) \quad (6)$$

where  $S_p(t)$  is the switching function,  $i_{lp}(t)$  represents the losses in the power circuit, and  $C_{eq}$  is the equivalent capacitor of the overall cluster  $p$  defined as  $C_{eq} = C/n$ . Since this study is focused on the low-frequency behavior of the system, the switching function is assumed to be  $S_p(t) = \tilde{S} \cos(\omega t + \phi_S)$ , by ignoring high-frequency components. When there is a dc current in the ac side, the STATCOM output current is  $i_p(t) = \tilde{I}_S \cos(\omega t + \phi_I) + \bar{I}_S$ . By substituting  $S_p(t)$  and  $i_p(t)$  in (6), it follows that

$$\begin{aligned} C_{eq} \frac{dv_{Cp}(t)}{dt} &= \tilde{S} \cos(\omega t + \phi_S) \cdot \\ &\times \left[ \tilde{I}_S \cos(\omega t + \phi_I) + \bar{I}_S \right] - i_{lp}(t) \\ &= \frac{\tilde{S} \tilde{I}_S}{2} [\cos(\phi_S - \phi_I) + \cos(2\omega t + \phi_S + \phi_I)] \\ &+ \tilde{S} \bar{I}_S \cos(\omega t + \phi_S) - i_{lp}(t) \end{aligned} \quad (7)$$

where a constant term, a line-frequency, and a double line-frequency ripples come out. By introducing a dc offset in the switching function  $S(t)$ , a degree of freedom is added able to reduce the dc current  $\bar{I}_S$ . Considering the switching function  $S_p(t) = \tilde{S} \cos(\omega t + \phi_S) + \bar{S}$  and substituting it in (6), it follows that the new dc-link voltage dynamics is

$$\begin{aligned} C_{eq} \frac{dv_{Cp}(t)}{dt} &= \left[ \tilde{S} \cos(\omega t + \phi_S) + \bar{S} \right] \cdot \left[ \tilde{I}_S \cos(\omega t + \phi_I) + \bar{I}_S \right] - i_{lp}(t) \\ &= \frac{\tilde{S} \tilde{I}_S}{2} [\cos(\phi_S - \phi_I) + \cos(2\omega t + \phi_S + \phi_I)] \\ &+ \tilde{S} \cdot \bar{I}_S \cos(\omega t + \phi_S) + \bar{S} \cdot \tilde{I}_S \cos(\omega t + \phi_I) + \bar{S} \bar{I}_S - i_{lp}(t) \\ &= \frac{\tilde{S} \tilde{I}_S}{2} \cos(\phi_S - \phi_I) + \bar{S} \cdot \bar{I}_S - i_{lp}(t) \\ &+ \tilde{S} \cdot \bar{I}_S \cos(\omega t + \phi_S) + \bar{S} \cdot \tilde{I}_S \cos(\omega t + \phi_I) \\ &+ \frac{\tilde{S} \tilde{I}_S}{2} \cos(2\omega t + \phi_S + \phi_I). \end{aligned} \quad (8)$$

By comparing (8) and (6), it turns out that, by adding the  $\bar{S}$  term, the constant term  $\bar{S} \cdot \bar{I}_S$  and the line-frequency ripple  $\bar{S} \cdot \tilde{I}_S \cos(\omega t + \phi_I)$  appear in the capacitor voltage dynamics. It is clear that the double line-frequency ripple is not affected by  $\bar{S}$ . Since this work refers to STATCOM, which aims to inject quadrature current, the relation  $\phi_I \simeq \phi_S \pm \pi/2$  holds. Hence, the line-frequency ripple in (8) is

$$\begin{aligned} &\tilde{I}_C \sin(\omega t + \phi_{Ic}) \\ &= \tilde{S} \cdot \bar{I}_S \cos(\omega t + \phi_S) + \bar{S} \cdot \tilde{I}_S \cos(\omega t + \phi_I) \\ &\simeq \tilde{S} \cdot \bar{I}_S \cos(\omega t + \phi_S) + \bar{S} \cdot \tilde{I}_S \cos(\omega t + \phi_S \pm \pi/2) \end{aligned}$$

$$\begin{aligned} &= \tilde{S} \cdot \bar{I}_S \cos(\omega t + \phi_S) \mp \bar{S} \cdot \tilde{I}_S \sin(\omega t + \phi_S) \\ &= \sqrt{(\tilde{S} \bar{I}_S)^2 + (\bar{S} \tilde{I}_S)^2} \sin\left(\omega t + \phi_S \mp \tan^{-1}\left(\frac{\tilde{S} \cdot \bar{I}_S}{\bar{S} \cdot \tilde{I}_S}\right)\right). \end{aligned} \quad (9)$$

It results that the injection of  $\bar{S}$  cannot reduce the amplitude of the line-frequency ripple, but it can reduce the constant part of the voltage dynamics in (8).

### B. Minimization of the DC Current

Section IV-A shows that an offset  $\bar{S}$  in the switching function  $S_p(t)$  affects the cluster voltage dynamics. This subsection shows that minimizing the error between the reference voltage  $V_{DC}$  and the cluster voltage  $v_{Cp}(t)$  is equivalent to minimizing the dc current  $\bar{I}_S$  in steady-state conditions. Hence, the cluster balancing algorithm satisfies two objectives simultaneously: it balances the voltage shared among the clusters and eliminates the dc component at the output current. Considering the system at steady-state condition, because of the effect of the upper voltage control level (the reference generator in Fig. 3), it is reasonable to assume  $v_{Cp}(t) \simeq V_{DC}$ . Therefore, a minimization of the error between  $V_{DC}$  and  $v_{Cp}(t)$  is equivalent to minimizing the dynamics in (6) enforcing  $dv_{Cp}(t)/dt \rightarrow 0$ . From (8), it is clear that  $\bar{S}$  cannot minimize the oscillating part and can only reduce the constant part. Thus, the following holds:

$$\begin{aligned} &\min_{\bar{S}} (v_{Cp}(t) - V_{DC})^2 \\ &\stackrel{\text{steady-state}}{=} \min_{\bar{S}} \left( C_{eq} \frac{dv_{Cp}(t)}{dt} \right)^2 \\ &= \min_{\bar{S}} \left( \frac{\tilde{S} \cdot \tilde{I}_S}{2} \cos(\phi_S - \phi_I) + \bar{S} \cdot \bar{I}_S - i_{lp}(t) \right)^2. \end{aligned} \quad (10)$$

By solving this optimization problem, the constant part is forced to approach zero, which enforces the law

$$\bar{S} = \left( i_{lp}(t) - \frac{\tilde{S} \cdot \tilde{I}_S}{2} \cos(\phi_S - \phi_I) \right) / \bar{I}_S \quad (11)$$

finally, establishing that increasing the dc offset  $\bar{S}$  in the switching function decreases the dc current  $\bar{I}_S$ . The result is that the dc current is attenuated by introducing an offset in the switching function with the aim to minimize the error between reference and cluster voltage.

### C. Cluster Voltage Balancing for MPC

From (3), the average capacitor voltages  $v_{Cp}$  across the three phases are

$$v_{Cp}(k+1) = v_{Cp}(k) + \frac{T_s}{C_{eq}} S_p(k) \cdot i_p(k), \quad p \in \{a, b, c\}. \quad (12)$$

The proposed third optimization layer aims to add a common-mode voltage to balance the cluster voltages of the three phases.

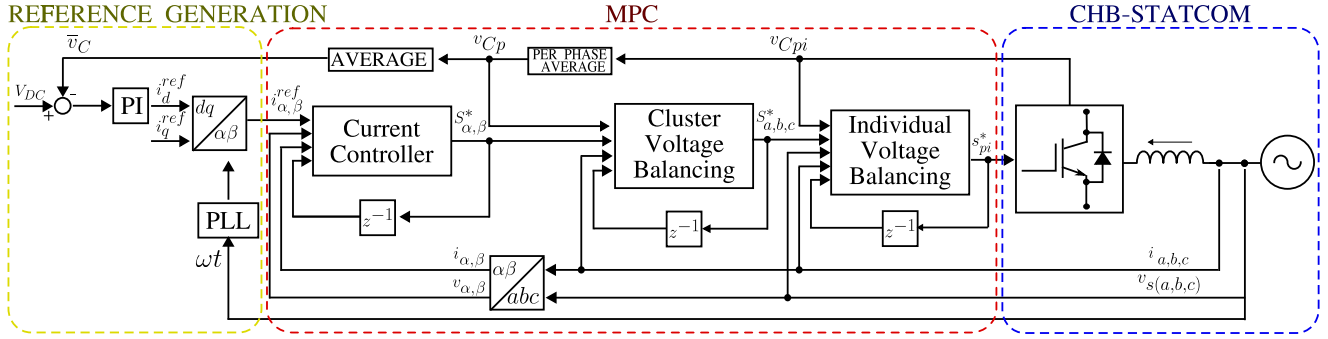


Fig. 3. CHB-STATCOM overall control scheme.

The cluster voltage balancing problem is as follows:

$$\begin{aligned}
 \min_{\mathbf{S}_{a,b,c}(k)} \quad & \left\| \mathbf{V}_{a,b,c}^{\text{DC}} - \mathbf{v}_{C(a,b,c)}(k+1) \right\|_{\mathbf{Q}_{cb}} \\
 & + \left\| \mathbf{S}_{a,b,c}(k) - \mathbf{S}_{a,b,c}(k-1) \right\|_{\mathbf{R}_{cb}} \\
 \text{s. t.} \quad & v_{Cp}(k+1) = v_{Cp}(k) \\
 & + \frac{T_s}{C_{eq}} S_p(k) i_p(k), p \in \{a, b, c\} \\
 & \mathbf{S}_{\alpha,\beta}^*(k) = \mathbf{T} \cdot \mathbf{S}_{a,b,c}(k) \\
 & \mathbf{S}_{a,b,c}(k) \in \mathbf{V}_{a,b,c}
 \end{aligned} \quad (13)$$

where  $\mathbf{V}_{a,b,c}^{\text{DC}} = [V_{\text{DC}}, V_{\text{DC}}, V_{\text{DC}}]^T$  and  $\mathbf{v}_{C(a,b,c)} = [v_{Ca}, v_{Cb}, v_{Cc}]^T$  are the  $3 \times 1$  vectors containing the reference voltages and the cluster voltages,  $\mathbf{S}_{a,b,c}$  is the switching vector in  $a, b, c$  coordinates,  $\mathbf{Q}_{cb}$  and  $\mathbf{R}_{cb}$  are tuning matrices. The first term is a weighted norm of the deviation of the three cluster voltages from the reference value. The second term is added to reduce the switching frequency. The matrix  $\mathbf{T}$  is the  $2 \times 3$  Clarke transformation matrix. The constraint in (13) is added to ensure that the injected common-mode voltage does not affect the  $\alpha, \beta$  currents controlled by the first optimization layer. In other words, the offset  $\bar{S}$  is introduced without affecting  $\bar{S}$ ,  $\phi_S$ ,  $\bar{I}_S$ ,  $\phi_I$  of (8). The algorithm can be simply implemented by searching among the  $2n+1$  redundant vectors in the  $a, b, c$  coordinates, as summarized in the flowchart in Fig. 4. The overall control scheme is summarized in Fig. 3.

## V. EXPERIMENTAL RESULTS

The proposed strategy was tested using a five-level CHB-STATCOM in Fig. 5, developed by DigiPower Ltd [28]. It consists of two H-bridges per phase, each one equipped with a dc-link capacitor. Each phase of the CHB-STATCOM is connected to the grid through a 230/80-V isolation transformer and a filter inductor. The CHB-STATCOM was designed based on [13] and, since MPC does not produce a fixed switching frequency, the filter inductor was sized based on the average frequency of the dominant high-order harmonics of the output voltage, which was about 8 kHz. The currents are sensed by three TDK CCT27-02 CTs. Table I summarizes the main parameters of the hardware components and the controller.

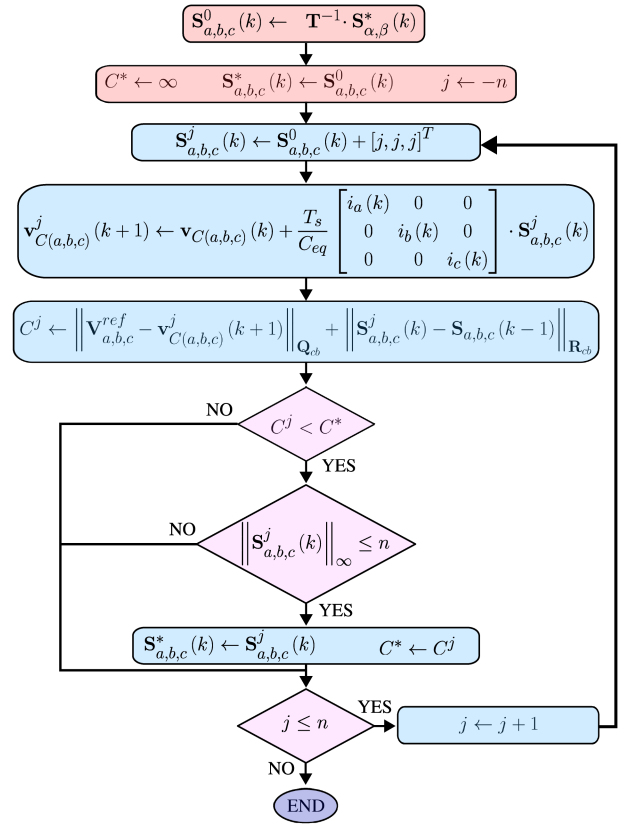


Fig. 4. Cluster balancing algorithm.

The system comprises a main board with an Intel Cyclone V 5CEBA7F31C8 FPGA, one external board for acquiring the grid voltage, and six H-bridges with the signal conditioning circuits to sample the dc-link voltages. Each H-bridge includes a Texas Instrument TMS320F28377SPTPT DSP for acquiring the measurements and sending them to the FPGA. Fig. 6 shows the schematic diagram of the experimental system and the overall controller was implemented on the FPGA. The PI reference generator in Fig. 3 was tuned based on [15] and the PI gains were set to 1 and 100, respectively. The MPC parameters were tuned using the empirical method in [22] and [23]. The current control was tuned to obtain a current total harmonic distortion (THD) of about 3%, the voltage balancing was tuned to ensure a maximum

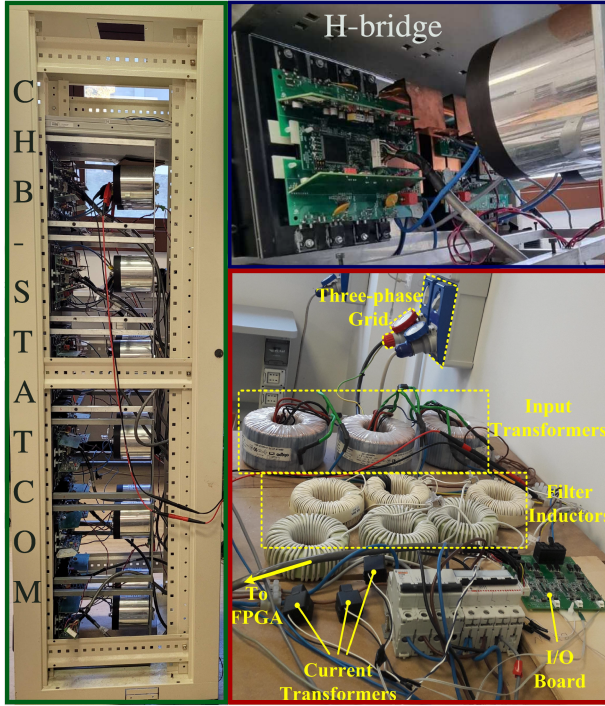


Fig. 5. Five-level CHB-STATCOM.

TABLE I  
PARAMETERS OF THE 5-LEVEL CHB-STATCOM

	Value		Value
PCC RMS voltage	80 V	$C$	0.9 mF
Grid frequency	50 Hz	$L$	6 mH
Rated power	$\pm 2$ kVAR	Inductor resistance $R$	0.5 $\Omega$
Number H-bridges per phase	2	Peak current	6 A
DC-link voltages	80 V	Sampling time $T_s$	50 $\mu$ s

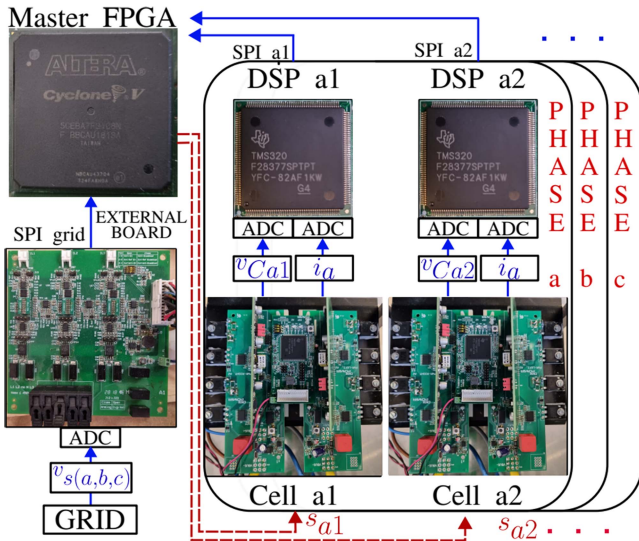


Fig. 6. Schematic diagram of the experimental setup.

TABLE II  
MPC CONTROL PARAMETERS

	$Q_i$	$R_i$	$Q_{ib}$	$R_{ib}$	$Q_{cb}$	$R_{cb}$
Value	$I_2$	$10^{-3} \times I_2$	$I_n$	$10^{-4} \times I_n$	$I_3$	$10^{-2} \times I_3$

TABLE III  
FOURIER ANALYSIS OF  $v_a(t)$ ,  $i_a(t)$ , AND  $\Delta v_{Ca}(t)$ .

	Without cluster balancing		With cluster balancing
$v_a(t)$ DC	0.49V	$v_a(t)$ DC	-71.93V
$v_a(t)$ 50 Hz	118.08 $\angle 3.82^\circ$ V	$v_a(t)$ 50 Hz	120.1 $\angle 2.28^\circ$ V
$v_a(t)$ 100 Hz	6.22 $\angle 0^\circ$ V	$v_a(t)$ 100 Hz	4.54 $\angle 0^\circ$ V
$i_a(t)$ DC	3.44 A	$i_a(t)$ DC	0.156 A
$i_a(t)$ 50 Hz	5.9 $\angle 89.09^\circ$ A	$i_a(t)$ 50 Hz	5.88 $\angle 89.19^\circ$
$i_a(t)$ 100 Hz	0.06 $\angle 0^\circ$ A	$i_a(t)$ 100 Hz	0.15 $\angle 0^\circ$ A
$\Delta v_{Ca}(t)$ DC	2.85 V	$\Delta v_{Ca}(t)$ DC	1, 12 V
$\Delta v_{Ca}(t)$ 50 Hz	9.5 $\angle -89.56^\circ$ V	$\Delta v_{Ca}(t)$ 50 Hz	9.15 $\angle 177.42^\circ$ V
$\Delta v_{Ca}(t)$ 100 Hz	4.04 $\angle 0^\circ$ V	$\Delta v_{Ca}(t)$ 100 Hz	4.07 $\angle 0^\circ$ V

voltage ripple of 10% and the cluster balancing guarantees a 0.5-p.u. dc offset, i.e., 0.3 A. Table II lists the weighting factors, where  $I_m$  is the  $m \times m$  identity matrix.

Fig. 7(a) shows the steady-state output voltage  $v_a(t)$ , current  $i_a(t)$ , and the error  $\Delta v_{Ca}(t) = (v_{Ca}(t) - nV_{DC})$  in cluster voltage when a 6-A peak quadrature current is given as reference without cluster balancing. The output voltage presents no dc offset, while a dc current appears in the output current. Fig. 7(b) shows the same waveforms when using the proposed cluster balancing. As shown, the extra control layer adds an offset in the output voltage that eliminates the dc current.

### A. Experimental Validation of the Theory

Fast Fourier transform analysis confirms the calculations in Section IV. Figs. 8–10 show, respectively, the Fourier spectrum of  $\Delta v_{Ca}(t)$ ,  $i_a(t)$ , and  $v_a(t)$ , and the amplitude and phase of the low-order harmonics are summarized in Table III.

Without the cluster balancing, the dc-link dynamics is given by (7). In steady-state conditions, the constant part of  $dv_{Ca}(t)/dt$  can be assumed to be zero. The switching function  $S_a(t)$  is equal to the output voltage over the nominal cluster dc-link voltage, i.e.,  $S_a(t) = v_a(t)/(n \cdot V_{DC})$ . Hence, substituting the numerical values obtained from experiments in Table III, it comes out that the current loss is

$$\begin{aligned}
 & \frac{\tilde{S} \cdot \tilde{I}_S}{2} \cos(\phi_S - \phi_I) \\
 & = -i_{la}(t) \Rightarrow i_{la}(t) = \frac{\tilde{S} \cdot \tilde{I}_S}{2} \cos(\phi_S - \phi_I) \\
 & i_{la}(t) = \frac{118.08}{160} \times 5.9 \text{ A} \cos(3.82^\circ - 89.09^\circ) = 0.179 \text{ A}.
 \end{aligned} \tag{14}$$

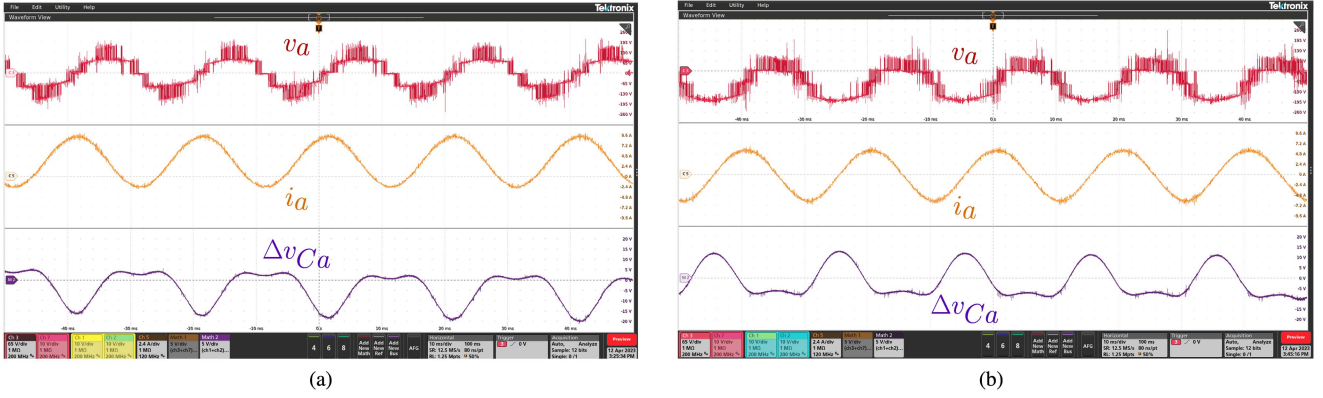


Fig. 7. CHB-STATCOM MPC without and with cluster balancing:  $v_a(t)$  [65 V/div],  $i_a(t)$  [2.4 A/div],  $\Delta v_{C_a}(t)$  [5 V/div], time [10 ms/div]. (a) CHB-STATCOM MPC without cluster balancing. (b) CHB-STATCOM MPC with cluster balancing.

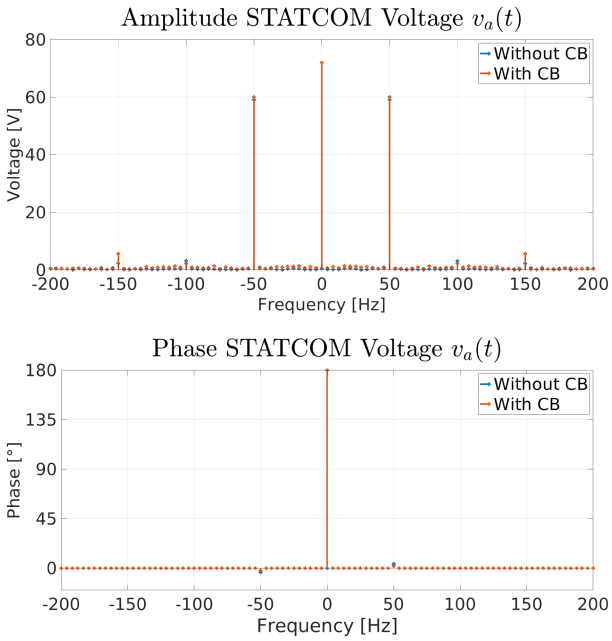


Fig. 8. Fourier spectrum of the output voltage.

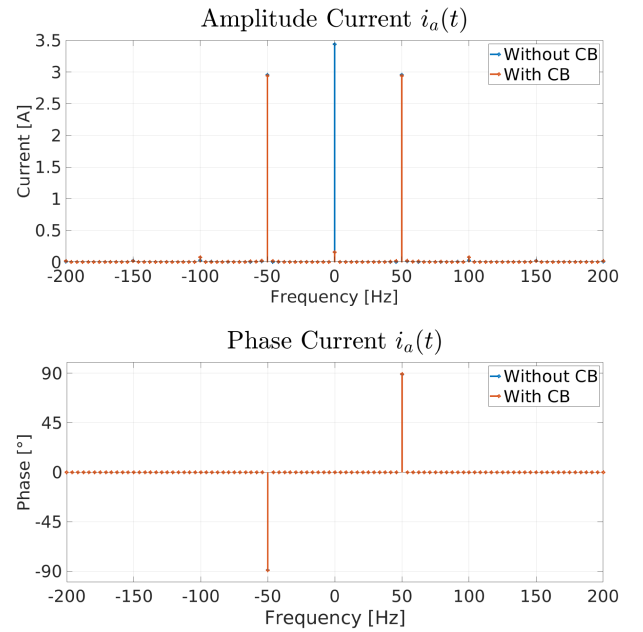


Fig. 9. Fourier spectrum of the output current.

From (7) the theoretical line-frequency ripple of the cluster is

$$\begin{aligned}
 \frac{1}{C_{eq}} \int_0^t \tilde{S} \cdot \bar{I}_S \cos(\omega\tau + \phi_S) d\tau &= \frac{\tilde{S} \cdot \bar{I}_S}{\omega C_{eq}} \sin(\omega t + \phi_S) \\
 &= \frac{\tilde{S} \cdot \bar{I}_S}{\omega C_{eq}} \cos\left(\omega t + \phi_S - \frac{\pi}{2}\right) \\
 &= \frac{118.08}{2 \times \pi \times 50 \times 0.9 \mu\text{F}} \times 3.44 \text{ A} \cos(\omega t + 3.82^\circ - 90^\circ) \\
 &= 9 \cos(\omega t - 86.18^\circ) \text{ V}
 \end{aligned} \tag{15}$$

which is very close to the measured  $9.5 \angle -89.56^\circ \text{ V}$ . When the cluster balancing control is introduced, the cluster voltage dynamics is (8). By considering the constant part of the new  $dv_{C_a}(t)/dt$  equal to zero and by substituting the values in

Table III, the following holds:

$$\begin{aligned}
 \frac{\tilde{S} \cdot \tilde{I}_S}{2} \cos(\phi_S - \phi_I) + \bar{S} \cdot \bar{I}_S - i_{la}(t) &= 0 \Rightarrow i_{la}(t) \\
 &= \frac{\tilde{S} \cdot \tilde{I}_S}{2} \cos(\phi_S - \phi_I) + \bar{S} \cdot \bar{I}_S \\
 i_{la}(t) &= \frac{120.1}{160} \times 5.88 \text{ A} \cos(2.28^\circ - 89.19^\circ) - \frac{71.93}{160} \\
 &\quad \times 0.156 \text{ A} = 0.17 \text{ A}
 \end{aligned} \tag{16}$$

where the theoretical loss current  $i_{la}(t)$  that is compensated is close to the one computed in (14). Indeed, in both scenarios, the dc current produced by the controller compensates the losses, forcing the cluster dynamics to be zero in steady state, verifying the assumption in (10). Substituting the experimental values in Table III into (9), the theoretical line-frequency ripple on the

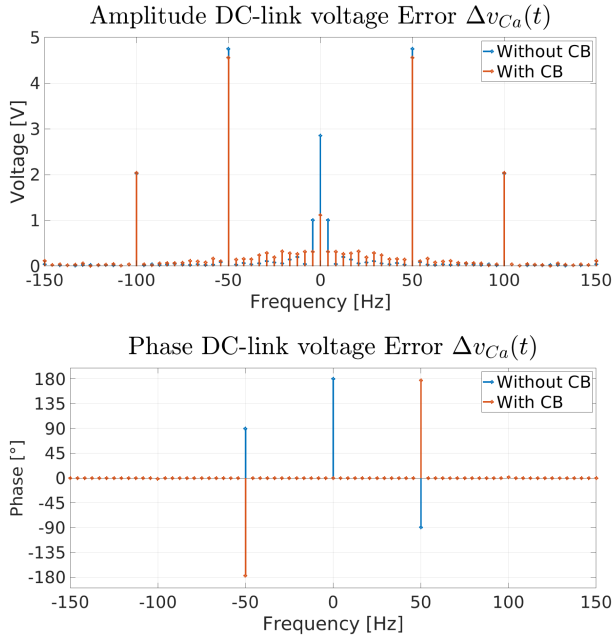


Fig. 10. Fourier spectrum of the dc-link voltage error.

TABLE IV  
PI CONTROL PARAMETERS

	Value		Value
$K_P$ current control	1	$K_I$ current control	100
$K_P$ voltage control	1	$K_I$ voltage control	0
$K_P$ dc elimination	0.5	$K_I$ DC elimination	10
Sampling time $T_s$	50 $\mu$ s	Carrier frequency	2 kHz

cluster is

$$\begin{aligned} \frac{1}{C_{eq}} \int_0^t \tilde{I}_C \sin(\omega\tau + \phi_{I_C}) d\tau &= -\frac{\tilde{I}_C}{\omega C_{eq}} \cos(\omega t + \phi_{I_C}) \\ &= 9.34 \cos(\omega t + 179^\circ) \end{aligned} \quad (17)$$

which is close to the experimentally measured  $9.15 \angle 177.42^\circ$ . Finally, according to Table III, the double line-frequency ripple in  $\Delta v_{C_a}(t)$  does not change by introducing the cluster balancing control. Indeed, the Fourier analysis verifies the theoretical reasoning presented in Section IV.

### B. Comparison With the Existing Method

The dc current elimination problem for CTs sensed CHB-STATCOM controlled by PI regulator was discussed in [9]. To the best of the authors' knowledge, the present work is the first one that faces this issue when using MPC. The standard PI control in [14] was implemented on the CHB-STATCOM prototype. To compare the proposed methodology with the PI strategy, the dc current elimination method in [9] was implemented and the steady-state, dynamic response, and computational burden were analyzed. The parameters of the PI control were tuned based on [9] and are listed in Table IV. The carrier frequency of the phase-shifted PWM (PSPWM) was set to 2 kHz to make a fair

TABLE V  
COMPARISON BETWEEN PI CONTROL AND MPC

MPC without dc current elimination		PI without dc current elimination	
$v_a(t)$ dc	0.49 V	$v_a(t)$ dc	0.48 V
$v_a$ THD	8.79 %	$v_a$ THD	35.48 %
$i_a(t)$ dc	3.44 A	$i_a(t)$ dc	2.73 A
$i_a(t)$ THD	58.02 %	$i_a(t)$ THD	46.78 %
MPC with dc current elimination		PI with dc current elimination	
$v_a(t)$ dc	-71.93 V	$v_a(t)$ dc	-25 V
$v_a$ THD	61.62 %	$v_a$ THD	39.17 %
$i_a(t)$ dc	0.156 A	$i_a(t)$ dc	0.23 A
$i_a(t)$ THD	4.12 %	$i_a(t)$ THD	6.06 %

comparison with the MPC, which had a compatible average switching frequency .

**1) Steady-State Performance:** Fig. 11(a) shows the output voltage, the current and the cluster ripple on phase  $a$  when controlling the CHB-STATCOM with a standard PI regulator. As expected, a dc current component appeared in the output current due to the CTs. Fig. 11(b) shows that the dc elimination method in [9] added a dc voltage on  $v_a(t)$  to compensate for the dc current on  $i_a(t)$ , and the ripple of the cluster  $\Delta v_{C_a}(t)$ , which was  $-90^\circ$  shifted with respect to  $v_a(t)$  [Fig. 11(a)], become  $+90^\circ$  shifted with respect to  $i_a(t)$  [Fig. 11(b)], as also happened with the MPC.

Fourier analysis and THD were computed to analyze the results, and the main parameters are summarized in Table V.

Both the proposed method and the method in [9] can suppress the dc current in the two different controllers by introducing a dc offset in the output voltage of the CHB-STATCOM. In the carried out test, the PI and the MPC experienced a 2.73 and 3.44-A current offset, resulting in a 58.02% and 47.78% current THD, respectively. By introducing the dc current elimination methods, a dc offset was injected in the output voltage of, respectively, -25 and -72 V, resulting in a THD of 61.62% and 39.17% for the two controllers, underlying that the output voltage was much distorted by the dc component in the MPC. Despite this, the dc current was 0.156 A with the MPC, against 0.23 A with the PI regulator, demonstrating the superior dc current suppression of the MPC. Moreover, the THD of the output current was 4.12% with the MPC and 6.06% with the PI, which confirmed the overall better performance of the MPC.

**2) Dynamic Performance:** To test the dynamic performance of the proposed method, the cluster balancing control was activated when a dc component was already present in the output current and compared with the PI method. Fig. 12 shows the dynamics of the current in a 10 s time window with a zoom before and after the activation of the dc elimination method for MPC [Fig. 12(a) and (c)] and PI [Fig. 12(b) and (d)]. Fig. 12(a) shows the MPC currents when the cluster balancing control was inactive and dc components appeared in the output currents of, respectively, 1.22, 1.2, and -2.54 A for phases  $a$ ,  $b$ , and  $c$ . At time 0 s, the cluster balancing control was activated and the dc component was gradually reduced and essentially eliminated at



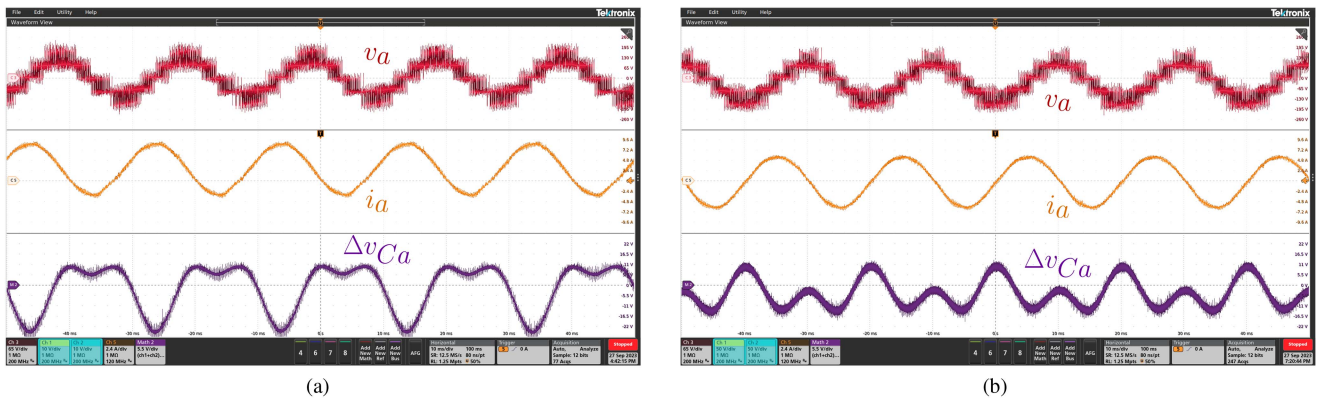


Fig. 11. DC current elimination method for PI-controlled CHB-STATCOM :  $v_a(t)$  [65 V/div],  $i_a(t)$  [2.4 A/div],  $\Delta v_{Ca}(t)$  [5.5 V/div], time [10 ms/div]. (a) PI-controlled CHB-STATCOM without dc current elimination method. (b) PI-controlled CHB-STATCOM with dc current elimination method.

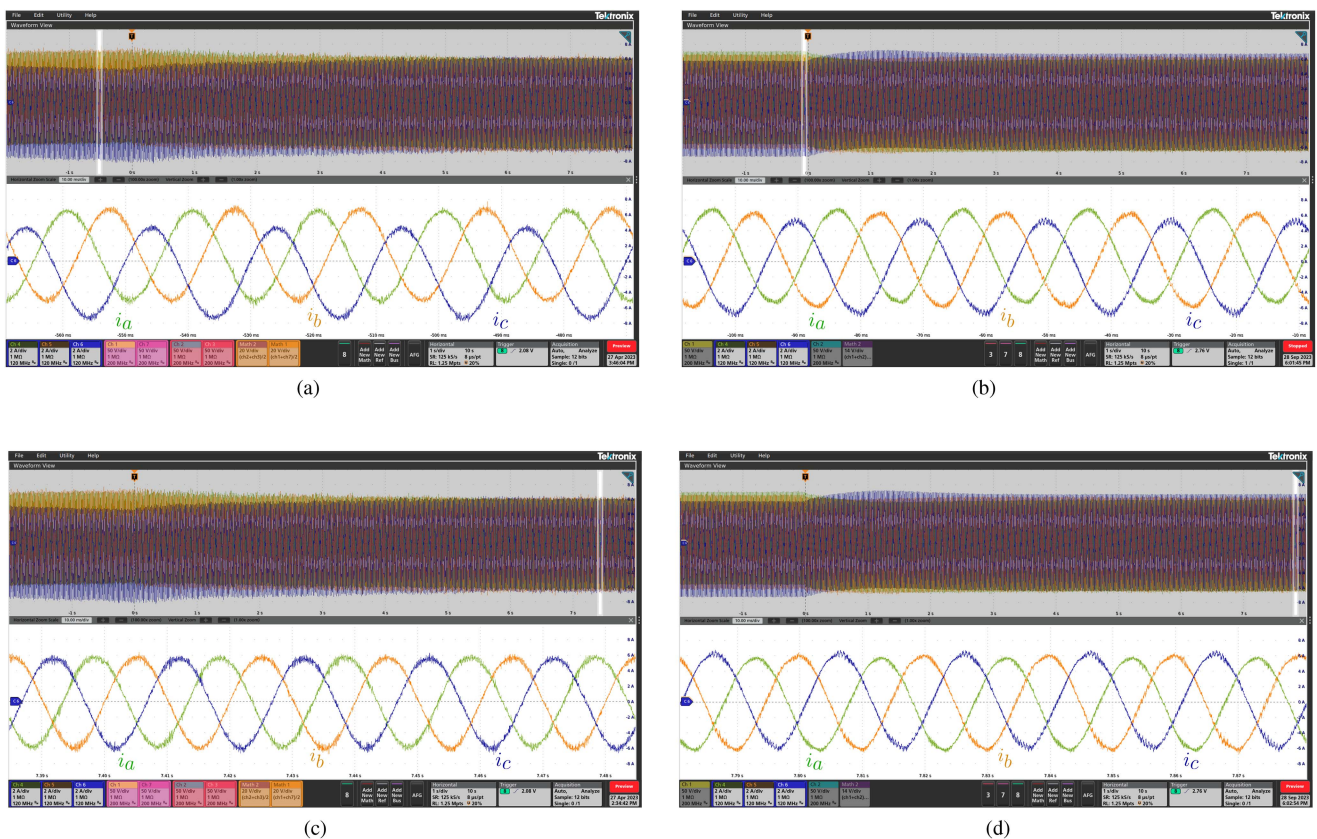


Fig. 12. CHB-STATCOM current dynamics (current [2 A/div], time [1 s/div]): at time 0 the dc elimination is activated. MPC before (Fig. 12(a)) and after (Fig. 12(c)) the activation of cluster balancing. PI before (Fig. 12(b)) and after (Fig. 12(d)) the activation of dc elimination. (a) STATCOM with MPC: zoomed view without cluster balancing (current [2 A/div], time [10 ms/div]). (b) STATCOM with PI control: zoomed view without dc elimination (current [2 A/div], time [10 ms/div]). (c) STATCOM with MPC: zoomed view with cluster balancing (current [2 A/div], time [10 ms/div]). (d) STATCOM with PI control: zoomed view with dc elimination (current [2 A/div], time [10 ms/div]).

time 5 s. Fig. 12(c) shows the output currents once they reached the steady state. The dc currents in the three phases were reduced to 0.12, 0.04, and  $-0.18$  A, respectively, which experimentally confirms the validity of the proposed approach.

The same test was carried out for the PI regulator and Fig. 12(b) shows the three-phase current for a standard PI control with a dc offset of 0.7, 0.25, and  $-0.84$  A for phases  $a$ ,  $b$ , and  $c$ .

At time 0 s, the dc current elimination method was activated and, after a 3-s transient, the offset was reduced to  $-0.37$ ,  $-0.13$ , and  $0.33$  A for phases  $a$ ,  $b$ , and  $c$ , as shown in Fig. 12(d). It is possible to note an overshoot before the dc current was suppressed, which is typical of PI regulators. The MPC with the proposed method had a better dc current suppression capability with respect to the PI control and, hence, a better current THD.

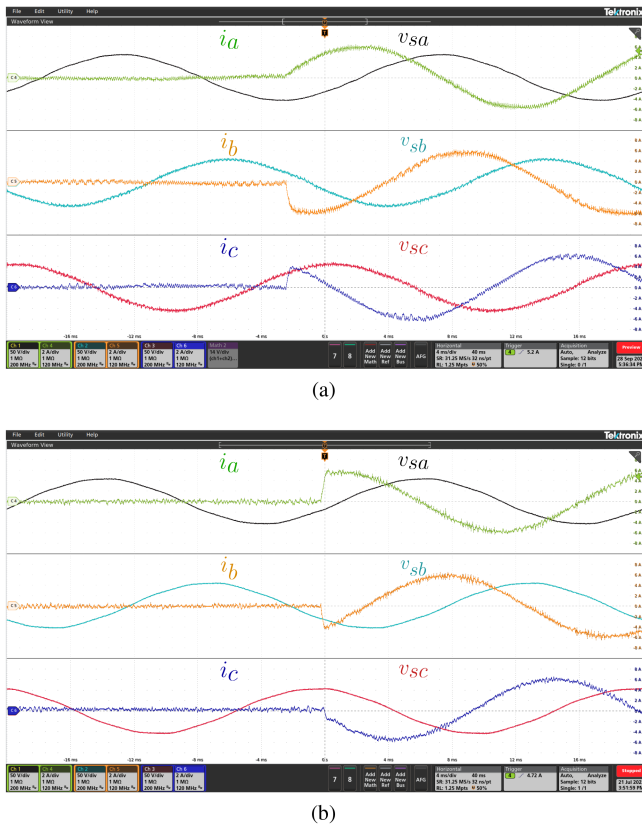


Fig. 13. Dynamic response of PI and MPC: voltage [50 V/div], current [2 A/div], time [4 ms/div]. (a) Dynamic response of PI control. (b) Dynamic response of MPC.

Fig. 13 shows the step response of the two controllers for a 6-A quadrature current reference. Both the dc current elimination methods did not substantially affect the step performance of the controllers while suppressing the dc component.

**3) Computational Burden:** The proposed cluster balancing algorithm in Fig. 4 was implemented on FPGA by fully exploiting the parallelism capability of the algorithm using three accumulators and three multipliers. By taking into account the possibility of computing up to three sums and multiplications in parallel and considering the required  $2n+1$  iterations, the number of clock cycles needed by the algorithm was  $12+16n$ , which resulted in  $0.92 \mu\text{s}$  for  $n = 2$  and 50-MHz FPGA clock frequency. The PI-based dc current elimination required computing  $a, b, c$  to  $d, q$  transformation, moving average filter and PI regulator for each phase, which resulted in  $1.12 \mu\text{s}$  with the same number of accumulators and multipliers. Therefore, both methods had a minor influence on the overall computational time. The current control of the FCS-MPC was implemented using the method in [27], which proposed a simple solution to the optimization problem by splitting the computations into three distinct steps. At first, a continuous unconstrained minimum problem is solved; then, the solution is projected into the hexagonal space to find the continuous constrained solution; finally, the discrete optimum is computed by searching between the two points close to the constrained solution. The algorithm in [27] is very efficient and

does not depend on the number of levels. The individual voltage balance algorithm was implemented, as described in [24]. The overall time spent for the FCS-MPC was  $12.34 \mu\text{s}$ , which was compatible with the  $11.4 \mu\text{s}$  spent by the overall PI control.

## VI. CONCLUSION

The FCS-MPC for CHB-STATCOM is usually addressed by dividing the overall optimization problem into the current control and the individual voltages balancing problem. This article proposes to add a third optimization layer to balance the voltages of the clusters by using the common-mode voltage. This article demonstrates that minimizing the clusters imbalance leads to the elimination of the dc current injected by the STATCOM. The proposed algorithm is simple to implement, requires few computations, and does not affect the ac output current. The experimental validation of the proposed solution was carried out with a five-level CHB-STATCOM employing CTs.

A comparison with a standard PI approach is given in terms of steady-state, dynamic performance, and computational burden, demonstrating the superior performance of the proposed technique.

## REFERENCES

- [1] S. Mohamadian, H. Pairo, and A. Ghasemian, "A straightforward quadrature signal generator for single-phase SOGI-PLL with low susceptibility to grid harmonics," *IEEE Trans. Ind. Electron.*, vol. 69, no. 7, pp. 6997–7007, Jul. 2022.
- [2] B. Long, M. Zhang, Y. Liao, L. Huang, and K. T. Chong, "An overview of DC component generation, detection and suppression for grid-connected converter systems," *IEEE Access*, vol. 7, pp. 110426–110438, 2019.
- [3] P. Ripka, K. Draxler, and R. Styblikova, "Measurement of DC currents in the power grid by current transformer," *IEEE Trans. Magn.*, vol. 49, no. 1, pp. 73–76, Jan. 2013.
- [4] S. N. Vukosavić and L. S. Perić, "High-precision active suppression of DC bias in AC grids by grid-connected power converters," *IEEE Trans. Ind. Electron.*, vol. 64, no. 1, pp. 857–865, Jan. 2017.
- [5] M. Armstrong, D. J. Atkinson, C. M. Johnson, and T. D. Abeysekera, "Auto-calibrating DC link current sensing technique for transformerless, grid connected, h-bridge inverter systems," *IEEE Trans. Power Electron.*, vol. 21, no. 5, pp. 1385–1393, Sep. 2006.
- [6] W. Zhang, M. Armstrong, and M. A. Elgendy, "Mitigation of DC current injection in transformer-less grid-connected inverters using a voltage filtering DC extraction approach," *IEEE Trans. Energy Conv.*, vol. 34, no. 1, pp. 426–434, Mar. 2019.
- [7] G. Qiu, J. Liao, B. Wu, and Z. Shi, "Suppressing DC current injection in transformerless grid-connected inverter using a customized current sensor," *IEEE Trans. Power Electron.*, vol. 36, no. 10, pp. 11003–11008, Oct. 2021.
- [8] Q. Yan, X. Wu, X. Yuan, Y. Geng, and Q. Zhang, "Minimization of the DC component in transformerless three-phase grid-connected photovoltaic inverters," *IEEE Trans. Power Electron.*, vol. 30, no. 7, pp. 3984–3997, Jul. 2015.
- [9] Y. Shi, B. Liu, and S. Duan, "Eliminating DC current injection in current-transformer-sensed STATCOMs," *IEEE Trans. Power Electron.*, vol. 28, no. 8, pp. 3760–3767, Aug. 2013.
- [10] M. Chen, D. Xu, T. Zhang, K. Shi, G. He, and K. Rajashekar, "A novel DC current injection suppression method for three-phase grid-connected inverter without the isolation transformer," *IEEE Trans. Ind. Electron.*, vol. 65, no. 11, pp. 8656–8666, Nov. 2018.
- [11] B. Guo et al., "Cost-effective DC current suppression for single-phase grid-connected PV inverter," *IEEE J. Emerg. Sel. Top. Power Electron.*, vol. 9, no. 2, pp. 1808–1823, Apr. 2021.
- [12] W. Zhang, M. Armstrong, and M. A. Elgendy, "DC injection suppression in transformer-less grid-connected inverter using a DC-link current sensing and active control approach," *IEEE Trans. Energy Conv.*, vol. 34, no. 1, pp. 396–404, Mar. 2019.

- [13] A. M. Saif, C. Buccella, V. Patel, M. Tinari, and C. Cecati, "Design and cost analysis for STATCOM in low and medium voltage systems," in *Proc. IEEE 44th Annu. Conf. Ind. Electron. Soc.*, 2018, pp. 3938–3943.
- [14] H. Akagi, S. Inoue, and T. Yoshii, "Control and performance of a transformerless cascade PWM STATCOM with star configuration," *IEEE Trans. Ind. Appl.*, vol. 43, no. 4, pp. 1041–1049, Jul./Aug. 2007.
- [15] D. Shetty and N. Prabhu, "Ziegler Nichols method based robust reactive current controller for STATCOM," *Energy Procedia*, vol. 117, pp. 543–550, 2017.
- [16] R. Xu et al., "A novel control method for transformerless H-bridge cascaded STATCOM with star configuration," *IEEE Trans. Power Electron.*, vol. 30, no. 3, pp. 1189–1202, Mar. 2015.
- [17] D. Lu et al., "Clustered voltage balancing mechanism and its control strategy for star-connected cascaded H-bridge STATCOM," *IEEE Trans. Ind. Electron.*, vol. 64, no. 10, pp. 7623–7633, Oct. 2017.
- [18] Y. Shi, B. Liu, Y. Shi, and S. Duan, "Individual phase current control based on optimal zero-sequence current separation for a star-connected cascade STATCOM under unbalanced conditions," *IEEE Trans. Power Electron.*, vol. 31, no. 3, pp. 2099–2110, Mar. 2016.
- [19] M. R. Nasiri, S. Farhangi, and J. Rodriguez, "Model predictive control of a multilevel CHB STATCOM in wind farm application using diophantine equations," *IEEE Trans. Ind. Electron.*, vol. 66, no. 2, pp. 1213–1223, Feb. 2019.
- [20] X. Pan, L. Zhang, Y. Li, K. Li, and H. Huang, "Modulated model predictive control with branch and band scheme for unbalanced load compensation by MMCC-STATCOM," *IEEE Trans. Power Electron.*, vol. 37, no. 8, pp. 8948–8962, Aug. 2022.
- [21] Q. Xiao et al., "Dual-layer modulated model predictive control scheme for the cascaded H-bridge converter," *IEEE Trans. Ind. Electron.*, vol. 70, no. 10, pp. 9751–9763, Oct. 2023.
- [22] P. Cortes et al., "Guidelines for weighting factors design in model predictive control of power converters and drives," in *Proc. IEEE Int. Conf. Ind. Technol.*, 2009, pp. 1–7.
- [23] P. Karamanakos and T. Geyer, "Guidelines for the design of finite control set model predictive controllers," *IEEE Trans. Power Electron.*, vol. 35, no. 7, pp. 7434–7450, Jul. 2020.
- [24] Y. Zhang, X. Wu, X. Yuan, Y. Wang, and P. Dai, "Fast model predictive control for multilevel cascaded H-bridge STATCOM with polynomial computation time," *IEEE Trans. Ind. Electron.*, vol. 63, no. 8, pp. 5231–5243, Aug. 2016.
- [25] Y. Zhang, X. Wu, and X. Yuan, "A simplified branch and bound approach for model predictive control of multilevel cascaded H-bridge STATCOM," *IEEE Trans. Ind. Electron.*, vol. 64, no. 10, pp. 7634–7644, Oct. 2017.
- [26] F. Simonetti, A. D'Innocenzo, and C. Cecati, "Neural network model-predictive control for CHB converters with FPGA implementation," *IEEE Trans. Ind. Inf.*, vol. 19, no. 9, pp. 9691–9702, Sep. 2023.
- [27] F. Simonetti, A. D'Innocenzo, and C. Cecati, "Simple explicit solution of finite control set model predictive control for cascaded H-bridge inverters," *IEEE Trans. Ind. Electron.*, pp. 1–11, 2023, doi [10.1109/TIE.2023.3321979](https://doi.org/10.1109/TIE.2023.3321979).
- [28] DigiPower, "DigiPower Website," 2023. Accessed: Sep. 25, 2023. [Online]. Available: <https://digipower.it/>



**Francesco Simonetti** (Student Member, IEEE) received the master's degree in control systems and computer engineering, in 2020, from the University of L'Aquila, L'Aquila, Italy, where he is currently working toward the Ph.D. degree with the Department of Engineering and Information Science and Mathematics.

His research interests include optimal control and machine learning techniques for multilevel converters.



**Sobhan Mohamadian** (Member, IEEE) received the B.Sc. and Ph.D. degrees in electrical engineering from the Iran University of Science and Technology, Tehran, Iran, in 2007 and 2016, respectively.

Between 2014 and 2015, he was a Visiting Scholar with the University of Trieste, Trieste, Italy, where he worked on research projects regarding high-power motor drives and multi-phase machine modeling and analysis. In 2016, he joined the University of Damghan, Damghan, Iran, where he was an Assistant Professor. Since 2022, he has been with the University of L'Aquila as an Assistant Professor conducting research plans on power electronics converters, renewable energy systems, and electrical machines drives.



**Concettina Buccella** (Fellow, IEEE) received the M.Sc. degree from the University of L'Aquila, L'Aquila, Italy, in 1988, and the Ph.D. degree in electrical engineering from the University of Rome "La Sapienza," Rome, Italy, in 1995.

From 1988 to 1989, she was a R&D Engineer with Italtel SpA, L'Aquila, Italy, then she joined the University of L'Aquila, where she is currently a Professor of Power Converters, Electric Machines, and Drives, and the Chair of B.Sc. in ICT Engineering. She is the Chief Scientific Officer with DigiPower Ltd., an R&D company active in the field of power electronics. Her research interests include modulation techniques for power converters, multilevel converters, reliability of power converters, analytical and numerical modeling of electric systems.

Dr. Buccella was the corecipient of the 2012 and the 2013 Best Paper Award of IEEE TRANSACTIONS ON INDUSTRIAL INFORMATICS. From 2017 to 2018, she was the Chair of the IEEE-Industrial Electronics Society Technical Committee on Renewable Energy Systems.



**Carlo Cecati** (Life Fellow, IEEE) received the Dr.Ing. degree in electrical engineering from the University of L'Aquila, L'Aquila, Italy, in 1983.

He has been a Professor of Industrial Electronics and Drives with the University of L'Aquila, since 2006. From 2015 to 2017, he was the Qianren Talents Professor with the Harbin Institute of Technology, Harbin, China. He is Chief Technical Officer with DigiPower Ltd., a power electronics research and development company. His research interests include power electronics, distributed generation, e-transportation, smart grids, and related technologies.

Dr. Cecati was the corecipient of the 2012 and 2013 IEEE TRANSACTIONS ON INDUSTRIAL INFORMATICS Best Paper Award, the 2012 *IEEE Industrial Electronics Magazine* Best Paper Award, and the 2019 IEEE TRANSACTIONS ON INDUSTRIAL ELECTRONICS Outstanding Paper Award. He was also the recipient of the 2017 Antony J. Hornfeck Award and the 2021 Eugene Mittlemann Achievement Award from the IEEE Industrial Electronics Society. From 2010 to 2015, he served as a Co-Editor-in-Chief and then Editor-in-Chief of IEEE TRANSACTIONS ON INDUSTRIAL ELECTRONICS.